Breakdown of Native Oxide Enables Multifunctional, Free-Form Carbon Nanotube−Metal Hierarchical Architectures

Kehang Cui*,[†,‡] and Brian L. Wardle*,[†]

[†]Department of Aeronautics and Astronautics, Massachusetts Institute of Technology, Cambridge, Massachusetts 02134, United States

[‡]School of Materials Science and Engineering, State Key Laboratory of Metal-Matrix Composites, Shanghai Jiao Tong University, Shanghai 200240, China

Ⓢ *Supporting Information*

ABSTRACT: Passive oxide layers on metal substrates impose remarkable interfacial resistance for electron and phonon transport. Here, a scalable surface activation process is presented for the breakdown of the passive oxide layer and the formation of nanowire/nanopyramid structured surfaces on metal substrates, which enables high-efficiency catalysis of high-crystallinity carbon nanotubes (CNTs) and the direct integration of the CNT−metal hierarchical architectures with flexible free-form configurations. The CNT−metal hierarchical architecture facilitates a dielectric free-energy-carrier transport pathway and blocks the reformation of passive oxide layer, and thus demonstrates a 5-fold decrease in interfacial electrical resistance with 66% increase in specific surface area compared with those without surface activation. Moreover, the CNT−metal hierarchical architectures demonstrate omnidirectional blackbody photoabsorption with the reflectance of 1×10^{-5} over the range from ultraviolet to terahertz region, which is 1 order of magnitude lower than that of any previously reported broadband absorber material. The synergistically incorporated CNT−metal hierarchical architectures offer record-high broadband optical absorption with excellent electrical and structural properties as well as industrial-scale producibility.

KEYWORDS: surface activation, catalysis, carbon nanotube, broadband absorber, energy storage
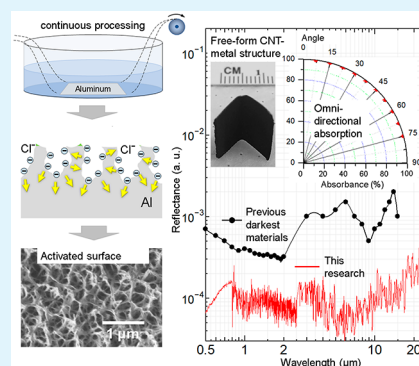
■ INTRODUCTION

Integration of carbon nanotubes (CNTs) with functional substrates offers synergistic mechanical robustness and physical properties, and thus is attractive for multipurpose applications,[1] such as energy conversion[2−4] and storage devices,[5−8] sensing, broadband absorbers,[9−11] flexible thermal interfaces,[12] electrical interconnects,[13] lightweight and deicing structural materials for aerovehicles,[14,15] etc. A universal challenge lies at the interface, where functional metallic substrates such as Al and Fe alloys would be passivated by a dense oxide layer upon exposure to the ambient,[16] which adds a remarkable barrier for electron and phonon transport. The drastic difference in terms of thermal expansion and Young's modulus between the metallic and oxide phases also deteriorates the mechanical integrity of the CNT-on-metal architecture. Lack of effective integration methods has been one of the major challenges limiting the large-scale applications of CNTs.

The conventional strategies for the integration of CNTs with functional metallic substrates include the transfer/bonding method and the direct synthesis method. For the transfer/bonding method, CNTs are detached from their growth substrates (e.g., Si/SiO₂) through oxidation, etching, etc., and are reassembled on the target substrates with intermediate layers, such as the transition metal carbide layer,[17] the covalent functionalization layer based on organic molecules,[18] and the brazing layer formed under high temperatures.[19] The transfer and bonding processes produce remarkable defects on CNTs and insert interfacial thermal/electrical barriers, both of which degrade the physical and chemical properties of the integrated CNT-on-substrate architecture. Moreover, high processing temperatures and additional materials are required, which increases the process complexity and cost significantly, and obviates the applicability to low working temperature substrates such as Al and Al alloys.

Enabling direct synthesis of CNTs on functional substrates at low temperatures is a promising direction to realize in situ device integration having compatibility and scalability for industrial applications. Al and Al alloys are lightweight, manufacturable, thermally and electrically conductive materials with the highest earth abundancy among metals and extremely low production cost, and thus are suitable substrate materials to integrate with CNTs.[20] The temperatures of direct synthesis of CNTs have already been reduced to below the melting temperature of Al (650−660 °C), yet the growth rate and yield of CNTs as well as the quality and graphitization level are far below those grown on Si wafers at temperatures over 750 °C,
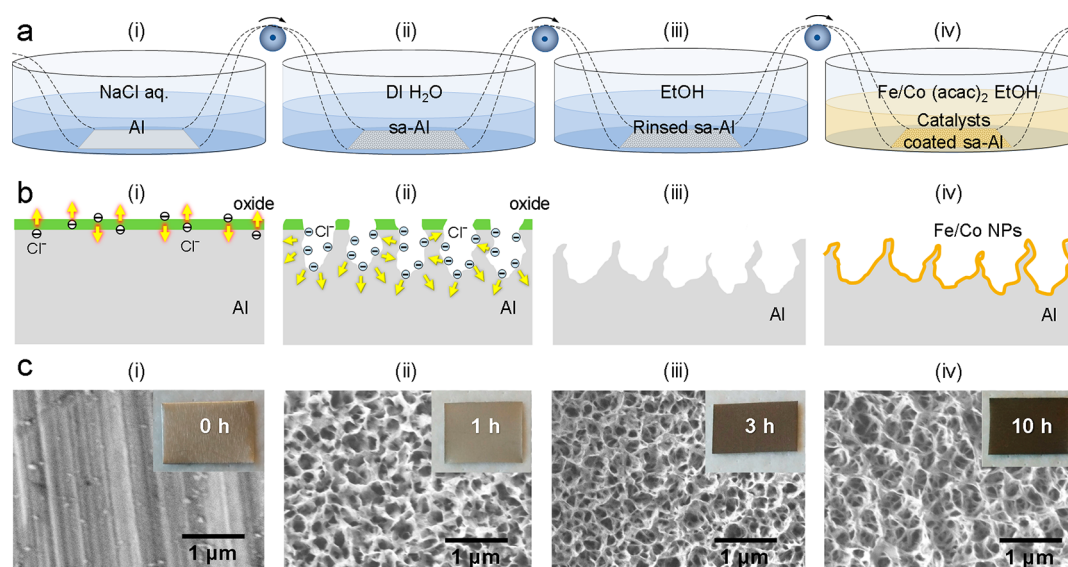
Figure 1. Solution-based surface activation (SA) process of Al substrate. (a) Process flow diagram. The Al substrate is submerged into NaCl aq. solution with sonication for surface activation, which removes the oxide layer and creates a nanostructured surface (i). The surface-activated Al (sa-Al) substrate is then rinsed in DI water (ii) and ethanol (iii). The Fe/Co catalysts for CNT synthesis are deposited on the rinsed sa-Al substrate by dip-coating in Fe and Co acetate ethanol solution and dried in reactor under Ar flow (iv). (b) Schematics of the surface structural evolution of the Al substrate. The surface activation is initiated by localized $\bar{Cl}$ attack (i). The oxide removal and nanostructure formation are realized by chloride accumulation and the associated fluctuations at the matrix/passive film interface (ii). After rinsing (iii), the sa-Al with superior wettability is coated with an Fe/Co acetate ethanol thin film (iv). (c) SEM images of the as-received Al substrate (i) and surface-activated Al substrates for different treatment duration of 1 (ii), 3 (iii), and 10 h (iv). The inset photo shows the color change of the corresponding Al substrates.

because of the low catalytic activity and severe subsurface element diffusion terminating the growth of CNTs. To mitigate these issues, oxide supporting layers, such as SiO_x,[21] AlO_x,[22] MgO,[23] and MoO_x[24] are deposited in between the catalyst layer and the substrate in previous studies to inhibit subsurface element diffusion and to form uniform catalyst nanoparticles to improve the yield and quality of CNTs. However, these oxide buffer layers are high-κ dielectrics which would aggravate electrical and thermal interfacial resistance. Moreover, the linear thermal expansion coefficient of the passive oxide layer (e.g., 7.2 μK^{-1} for Al_2O_3) and the Al substrate (24 μK^{-1}) can cause delamination of CNTs from the Al substrate during the synthesis process.[25]

Here we present a scalable and environmentally benign surface activation (SA) process to break down the passive oxide film and achieve direct synthesis and integration of high-crystallinity CNTs/surface-activated Al (CNT/sa-Al) substrate for omnidirectional, broadband absorber with excellent structural and electrical properties. The SA process of the Al substrate is inspired by the attack of chlorine anions on the surface of metals in aqueous solutions which induces modification of the surface on Al and Al alloys. Here, the SA process plays two roles, (1) to remove the oxide layer and expose metallic surface for direct contact between CNTs and Al substrate, and (2) to create a nanostructured surface to enable high catalyst loading and catalytic activity at low temperatures. Moreover, the SA process can be implemented by a scalable roll-to-roll setup for free-form flexible substrates for industrial-scale production.

■ EXPERIMENTAL SECTION

Surface Activation of Al and Catalyst Deposition. Two kinds of materials are used. The Al alloy sheet with thickness of 500 μm (Alcoa 4 series) and Al metal foil with thickness of 2 μm (Reynolds). The Al alloy contains 0.6 wt % Si, 1.2 wt % Mn, 0.6 wt % Zn, 0.3 wt %

Fe, and 0.26 wt % Cu. The Al alloy sheet and Al metal foil were immersed in 10 wt % NaCl aqueous solution with bath sonication until the desired structure was obtained. The activated Al substrate were rinsed by DI water and ethanol (99.5%, Sigma-Aldrich) and subsequently immersed into catalyst solution before drying. The catalyst solution contains 0.1 M iron(II) acetate and 0.1 M cobalt(II) acetate in ethanol.

Low-Temperature CNT Synthesis. The CNT structures were synthesized by oxygen dehydrogenation reaction (ODR) using a home-built setup, a.k.a. Mango Tango. Before synthesis, the activated Al substrate loaded with catalyst solution was dried in a quartz tube with 1000 sccm Ar flow to avoid the formation of oxide. The substrate was then heated to a preset temperature (ranging from 400 to 600 °C) and kept for 10 min under 400 sccm H_2 (Airgas) and 100 sccm Ar (Airgas). CNTs were grown using 167 sccm 10% C_2H_2 diluted in Ar and 17 sccm CO_2 and 800 sccm Ar for typically 30 min. After growth, the sample was cooled to room temperature under 1000 sccm Ar flow.

Catalyst and CNT Characterization. The morphologies of Al substrate and CNTs were observed by Zeiss Merlin SEM with Gemini II column. Atomic structures of CNTs and catalysts were observed by JEOL 2010 Advanced High Performance TEM operating at 200 kV with a lanthanum hexaboride cathode. The surface chemical status of activated Al and catalysts were carried out using Physical Electronics Versaprobe II X-ray Photoelectron Spectrometer. Raman spectra of CNTs were performed by Horiba Jobin Yvon model HR800, using 532 nm laser excitation.

Electrical and Optical Properties Characterization. The optical properties were measured by UV−vis−NIR transmission/reflectance spectrophotometer (Varian/Cary-5000) using a commercial reference aluminum coated mirror (Thorlabs). The angular dependence of the optical properties was measured using a variable angle spectral reflectance accessory (VASRA). The Brunauer−Emmett−Teller surface area analysis was performed by Micromeritics ASAP2020 using Kr as absorbate gas. The weight of the CNTs is obtained by measuring the difference in weight of the substrate before and after growth of multiple samples to achieve the required standard error. The impedance and electrical properties of CNT-Al structure were characterized by Solartron 1287A.
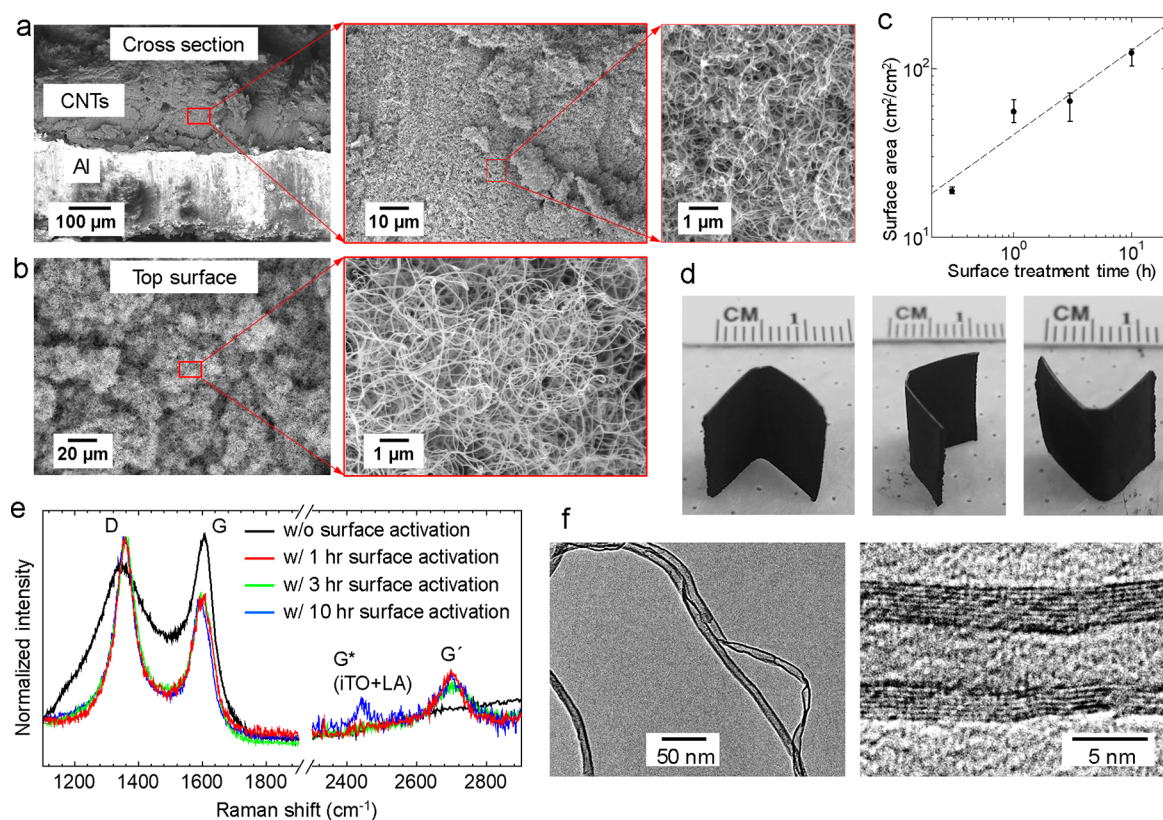
Figure 2. Characteristics of crystalline high-yield CNTs synthesized directly on metallic sa-Al substrate. (a, b) SEM images of top surface (a) and cross-section (b) of the CNTs. (c) Areal surface area of CNTs on sa-Al with different surface activation treatment times. (d) Photograph of the freeform CNT-Al structure synthesized in a 1 in. furnace. (e) Raman spectroscopy of the CNTs synthesized on nontreated Al substrate and sa-Al substrate with different surface activation times. (f) Representative TEM image of the synthesized CNTs.

◼ RESULTS AND DISCUSSION

Figure 1a shows the fully solution-based SA process that is applicable to complex-shaped Al substrates and scalable for large-area industrial production through implementation in an automated continuous production system. The Al substrates (applicable to both sheets and foils) are sonicated in 10 wt % NaCl aq. solution for 10 min for in-depth penetration of $\overline{Cl}$ and the initiation of the breakdown of the native Al oxide layer. Then the Al substrates are soaked in the same NaCl solution until the native oxide layer is fully removed and the desired nanostructured surface is formed. As shown in Figure 1b, the SA process of the Al substrate in an aqueous solution with $\overline{Cl}$ follows three steps. (i) The chlorine ions incorporate in the oxide layer and permeate through the inner metallic bulk. (ii) The undulation of the accumulated chloride ions induces localized attack on the oxide layer, resulting in the breakdown of the oxide layer and dissolution of the metallic Al bulk in contact with the aqueous solution, and later formation of metastable pit structures.[26] The breakdown of the passive oxide layer and the metastable pits would accelerate the surface activation process.[26] (iii) The metastable pits later develop into arrays of nanowire/nanopyramid hybrid structures with the size of 20−50 nm. The morphological evolution of the surface-activated Al substrates is shown by the SEM images in Figure 1c. With elongation of the surface treatment time, the metastable pits are interconnected owing to the enlargement of the pores, forming a random network of Al nanowires with the average diameter of ca. 20 nm after 10 h surface activation treatment. The change in the surface roughness is reflected by

the structural color change of the substrate, as shown by the photographs in the inset of Figure 1c. The glossy metallic color of the as-received Al substrate (i) gradually fades with the increase of the SA treatment time (ii, iii), and eventually turns into black (iv) owing to the plasmonic resonance of Al nanostructures.[27]

After the SA process, the sa-Al substrate is thoroughly rinsed using DI water and ethanol. The nanoporous structures on sa-Al substrates enable excellent wettability for both water and ethanol, resulting in uniform liquid film coating during the rinsing process which prevents the exposure of the sa-Al to the ambient. The bimetallic Fe/Co catalysts are deposited on the sa-Al substrate through dip-coating in 0.1 M ethanol solution of iron(II) and Co(II) acetates. The solution-covered sa-Al substrate is immediately transferred into the CVD chamber and dried under 1000 sccm He flow to prevent direct exposure to air and thus avoids the near-instant formation of the native oxide layer. The nanoporous structures on sa-Al could significantly improve the catalyst loading and distribution uniformity through capillary effect (Figure 1b (iv)).

We employ a high-fidelity catalysis approach for low-temperature CNT growth based on the oxidative dehydrogenation reaction (ODR) of acetylene. Here extra CO_2 is used with the molar stoichiometry of 1.03:1 to C_2H_2 as a growth enhancer which etches away the amorphous carbon formed at lower temperatures for the alleviation of catalyst poisoning and removal of amorphous carbon during growth. The representative SEM images in Figure 2a (top surface) and b (cross-section) demonstrate that the morphology of CNTs produced by the ODR at 500 °C is a dense and randomly networked
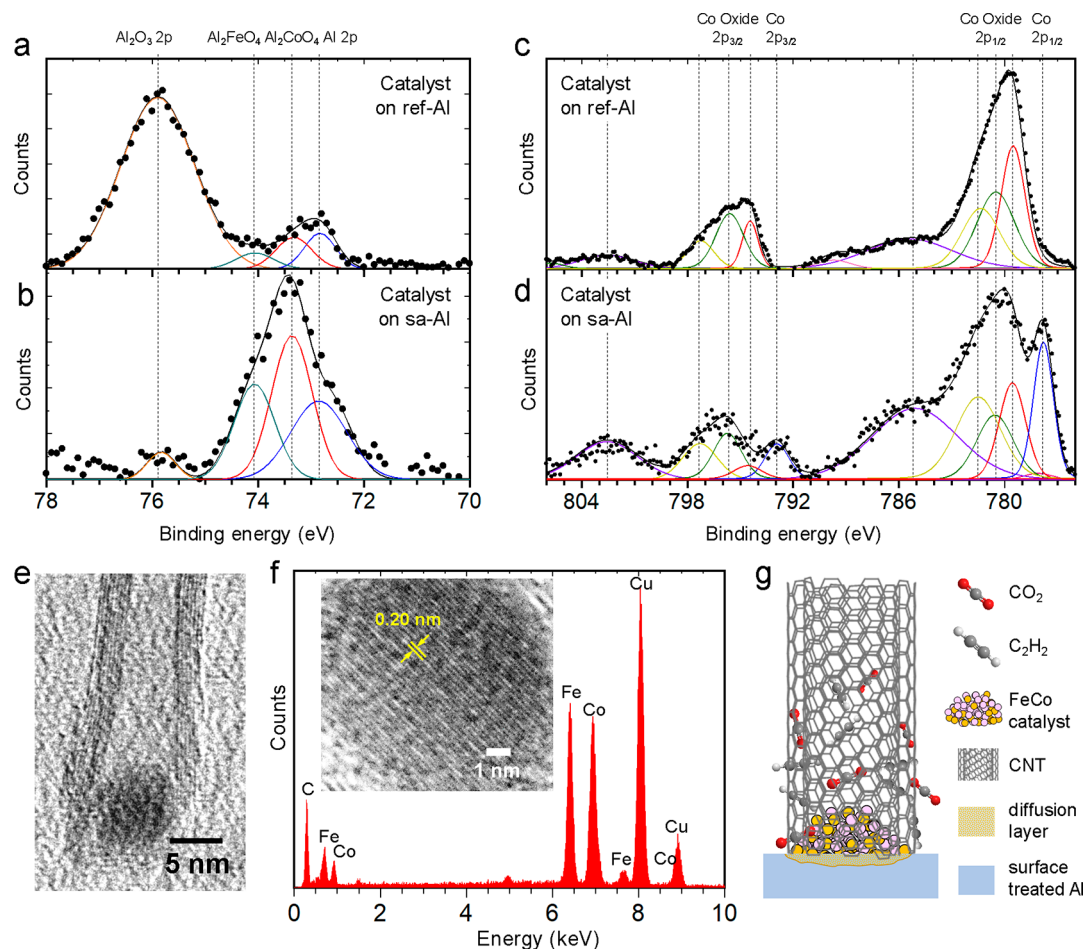
Figure 3. Catalyst analysis of low-temperature CNT synthesis on Al substrate. (a, b) Al 2p XPS spectra of the Al substrates without (a) and with (b) surface activation. (c, d) Co 2p1/2 and 2p3/2 XPS spectra of the annealed catalysts on Al substrate without (c) and with (d) surface activation. The catalysts were annealed under the same condition of the oxygen dehydrogenation reaction (ODR) process without flowing of carbon precursor. (e) Representative TEM image of catalyst nanoparticle inside a CNT. (f) Lattice distance and EDS-TEM analysis of FeCo alloy catalyst scratched from the sa-Al substrate after ODR synthesis of CNTs. (g) Schematics of the ODR process for CNT synthesis on the sa-Al substrate.

mat, because of the nanostructured surface of the sa-Al substrate. The thickness of the CNT forest achieves 500 μm after a 30 min ODR growth process, with the growth rate an order of magnitude faster than the previous reported values.[28,29] The CNT yield, as quantified by the areal surface area (measured using Brunauer−Emmett−Teller (BET) analysis) in Figure 2c increases monotonically with the elongation of SA treatment time on the log−log scale, which could be attributed to the fractal growth of metastable pits on the Al substrates by the SA process.[26,30] The high-yield ODR synthesis of CNTs is realized at low temperatures over a broad window from 400 to 600 °C (Figure S1). As the catalytic activity is proportional to the number of active sites, the SA process presented in this research can be used as a universal strategy to enhance catalysis processes.

The SA process can be exploited for flexible and free-form configurations of CNT-metal architectures. Figure 2d shows the uniform CNT synthesized on sa-Al substrates that are bended for more than 90°. Utilizing the flexibility of Al substrate and the wider-range growth temperature window, we synthesize CNTs on an sa-Al foil substrate with 6-in. diameter in a 1 in. tube furnace by rolling (Figure S2). For the Al foil substrate without surface activation, the morphology of as-synthesized CNTs is sparsely distributed spots after 10 min of

the ODR growth process (Figure S3). The thermal-expansion mismatch induced delamination of CNTs from the Al substrates after 2 h of the ODR process is also observed for the nontreated substrate, which causes premature termination of the growth (Figure S4). The SA process provides flexibility in the design of continuous CNT-on-Al manufacturing system and overcomes the extreme susceptibility to reaction temperature that has been one of the major issues hindering the scalable and uniform synthesis of CNT−metal architectures.

Raman spectra in Figure 2e (and Lorentzian-curve fitting in Figure S5) show that the G/D ratio of the CNT grown on the sa-Al substrate is improved by 4-fold compared with that of the CNT grown on reference Al. Moreover, G' band of the CNT grown on the sa-Al substrate is clearly defined, demonstrating a low defect level and high crystallinity. The peaks located at 1150 and 1450 cm^{-1} representing the amorphous sp^3 carbon[31,32] are also quenched. Elongation of the SA treatment time could further improve the graphitization level and purity of the as-synthesized CNTs, as shown by the appearance of the nondispersive G* band located at ~2450 cm^{-1}. The TEM images in Figure 2f shows the high-crystalline graphitic layers of the CNTs synthesized on the sa-Al substrate, with average wall number of 6−8 and diameter of 10 nm; while the CNTs synthesized on the non SA-treated Al are highly defective with
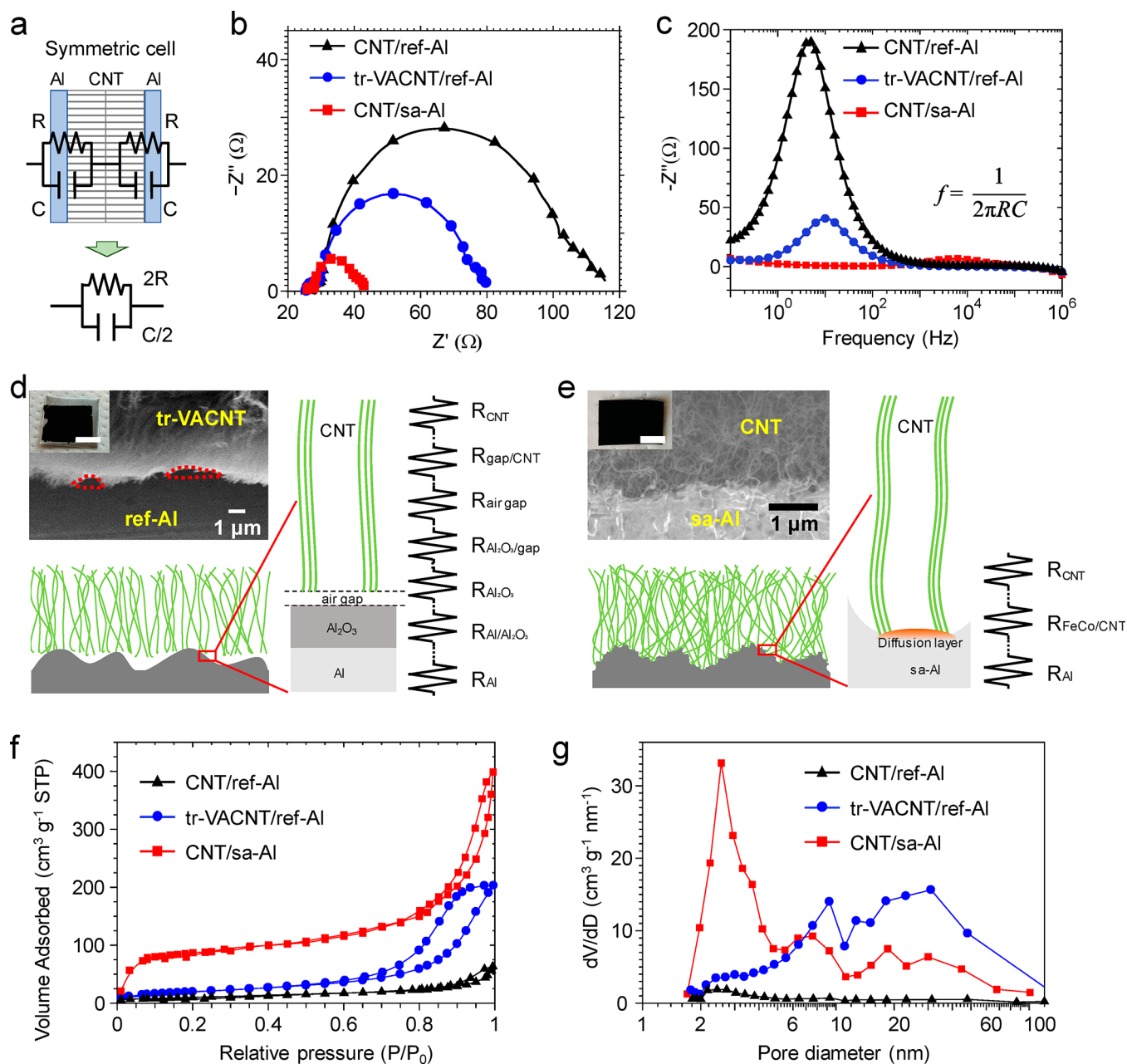
Figure 4. Physical properties of oxide-free CNT/sa-Al architecture. (a) Schematic of symmetric test setup for impedance measurement. (b) Nyquist plot and (c) Bode plot of ref Al, VACNT/ref Al and CNT/sa-Al hierarchical structures. (d) SEM image of the cross-section of the tr-VACNT/ref-Al sample with the inset showing the photograph of the sample. The dashed red circles denote the local gaps between the VACNT and Al substrate. The schematics shows the interface of the tr-VACNT/ref-Al and its equivalent circuit of electron transport. (e) SEM image and schematics of the cross-section of the CNT/sa-Al sample with the inset showing the photograph of the sample. (f) Pore distribution and (g) surface area of the ref Al, VACNT/ref Al and CNT/sa-Al hierarchical structures using Brunauer−Emmett−Teller (BET) analysis.

low-graphitization turbostratic fishbone structures and a larger diameter of 20 nm (Figure S6). The TEM images corroborate the Raman spectra, demonstrating the crystallinity of CNTs synthesized on the sa-Al substrate at 500 °C are comparable to that of the wafer-grown CNTs at temperatures over 750 °C.

The chemical status of the activated surface was probed by X-ray photoelectron spectroscopy (XPS) to investigate the mechanism of the simultaneously enhanced yield and crystallinity of CNTs at low synthesis temperatures. As shown by the Al 2p XPS curves in Figure 3a, b, the as-received Al substrate has strong oxide peak (75.9 eV) because of the dense native oxide, whereas this oxide peak almost

disappears for the sa-Al substrate, demonstrating the efficacy of the SA process for the breakdown of the native oxide layer. The exposed metallic Al surface allows sufficient element diffusion, and thus results in the formation of the Al-rich intermetallic compounds (73.6 eV for Al_2CoO_4 and 74.3 eV for Al_2FeO_4) that are reported to be effective catalytic-active centers for dehydrogenation.[33−35] Moreover, the exposed metallic Al surface serves as a solid-state reducing agent[34] for the catalyst during the annealing process. As shown by the XPS spectra in Figure 3c, d, the 2p 1/2 (793.3 eV) and 2p 3/2 (777.8 eV) XPS peaks of the metallic Co phase emerge after annealing for the sa-Al substrate, while the Co phase for the

nontreated sample is completely oxide. Moreover, the nanostructured Al with large surface area and high wettability enables trapping of catalyst atoms and uniform dispersion of catalyst particles,[36,37] and enhances hydrogen adsorption and spillover onto catalysts,[38,39] both of which contribute to the enhanced catalytic activity at lower CVD temperatures.

The exemplary TEM image in Figure 3e shows that the average diameter of the catalyst nanoparticle is *ca.* 6 nm, which matches that of the CNTs, demonstrating a characteristic tangential growth mode.[40] The catalyst nanoparticle is mainly composed of Fe and Co, as shown by the EDS-TEM analysis in Figure 3f. The exemplary high-resolution TEM image in the inset of Figure 3f shows the lattice distance of the catalyst nanoparticle is 0.20 nm, matching those of the Fe−Co intermetallic compounds (FeCo and $Fe_{0.72}Co_{0.28}$). For the Fe−Co bimetallic catalyst, the subsurface elemental diffusion is significantly alleviated, with a large amount of Fe−Co retained on the surface after annealing at 500 °C for 30 min; whereas monometallic Co and Fe peaks completely disappear after annealing (XPS survey spectra in Figure S7). This is attributed to the anchoring effect of the Fe−Co intermetallic compounds.[41,42] The schematic of the high-quality direct synthesis of CNTs on the surface-activated Al substrate is shown in Figure 3g. The bimetallic catalyst substantially lowers the activation energy for CNT synthesis[42−44] and maintains high catalytic activity at relatively low temperatures.

To characterize the interface resistance between CNTs and Al substrates, we fabricate symmetric cells using two identical samples synthesized by the same condition as shown in Figure 4a, and use electrochemical impedance spectroscopy (EIS) to analyze the interface resistance between CNTs and the Al substrate. We transfer a reference VACNT forest onto the Al without SA process (tr-VACNT/ref-Al) as a baseline to compare with as grown CNT/sa-Al and CNTs grown directly on reference Al (labeled as CNT/ref-Al). The detailed process for the synthesis of reference VACNTs can be found in our previous publications.[45] To prepare the tr-VACNT/ref-Al sample, we first delaminated VACNTs grown on SiO_2/Si substrate at 750 °C from the growth substrate by annealing in hydrogen (50 sccm) and helium (200 sccm) environment. Hydrogen could react with the amorphous carbon and carbon chains attached around the catalysts, which was generated during the CVD process. The delaminated free-standing VACNTs are carefully transferred onto reference Al substrate. The stacked tr-VACNT/ref-Al structure is annealed under a minor pressure at 500 °C in helium environment to enhance the contact at the interface. The SEM image of the tr-VACNT/ref-Al (Figure S8a) illustrates that the vertical alignment was well maintained from the as-synthesized VACNTs. However, even though the applied pressure during the annealing process partially breaks the vertical alignment near the bottom (Figure S8b), local gaps between the tr-VACNT and ref-Al are still inevitable, because of the inherent submicron roughness of both the as-synthesized VACNTs and the Al substrate and their distinct mechanical properties.

Figures 4b, c respectively present the corresponding Nyquist and Bode plots of symmetric cells based on CNT/sa-Al, tr-VACNTs/ref-Al, and CNT/ref-Al. Through curve fitting using the equivalent circuit shown in Figure 4a, the charge transfer resistance of the CNT/sa-Al interface is calculated as ca. 0.5 Ω/cm^2, which is 5-fold lower than that of the tr-VACNT/ref-Al, and an order of magnitude lower than that of the CNT/ref-Al samples. The frequency shift in the Bode plot demonstrates

faster electron transfer at the interface between CNTs and the conductive substrate because of the oxide removal by the SA process. The conductive paths of the charge carriers for tr-VACNT/ref-Al and CNT/sa-Al samples are compared in Figure 4d, e. The zoom-in cross-sectional SEM images clearly show that local gaps on the order of 100 nm are distributed across the interface between tr-VACNT and ref-Al; while for the CNT/sa-Al sample, each CNT are in direct contact with the sa-Al substrate, even though the surface roughness of sa-Al is much greater than that of the ref-Al substrate. The air gap in the tr-VACNT/ref-Al sample adds substantial ohmic and interface resistance in the equivalent circuit for both electrons and phonons. Filler materials, such as conductive polymers[18] or metals,[19] could be used to mitigate the ohmic resistance of the air gap, however, the interface resistance still remains with increased fabrication cost and process complexity. Moreover, the direct contact between metallic Al substrate and as-synthesized CNTs potentially block the reformation of the dense and continuous passive oxide layer, of which the growth occurs instantly in the ambient and cannot be removed. The high-quality CNTs, the catalyst diffusion layer and metallic bulk Al substrate form conductive pathway for electrons and phonons which bypasses the high-κ dielectric layers of air gaps and native oxide with minimum interfaces. The CNT/ref-Al sample does not have air-gap but the resistance in the low-quality turbostratic CNT is dominant (Figure S9).

The surface area of the CNT-Al samples was characterized by the Brunauer−Emmett−Teller (BET) analysis. Figure 4f presents the N_2 sorption/desorption isotherms of the CNT-Al samples, with the pore size and cumulative sorption volume data. The type IV isotherms have negligible hysteresis, which is evidence of the porous structure predominantly formed by mesopores. The CNT/sa-Al hierarchical architecture possesses a surface area of 245.7 m^2/g, which is 65.8% larger than that of the tr-VACNT/ref-Al sample. The broad knee in the low P/P_o range and well-defined plateaus of adsorbed volume further indicate the existence of numerous mesopores and micropores for the CNT/sa-Al sample. Figure 4g indicates a bimodal pore size distribution, with the majority as small pores ranging from 2−5 nm and a small portion as medium pores ranging from 30−50 nm for the CNT/sa-Al hierarchical architecture. The bimodal pore size distribution may facilitate the rapid and complete adsorption/desorption, and prevent the H_3 hysteresis loop in the reference CNT forest transferred on the Al substrate. The extremely low interface electrical resistance combined with the excellent pore structure makes the oxide-free CNT-Al structure an ideal candidate hierarchical functional structure for energy-storage applications such as batteries[46] and supercapacitors.[47]

VACNT forests have long been considered as a promising candidate for broadband omnidirectional absorber for astronomic telescope, sensing, and solar energy conversion because of the intrinsic properties of graphitic material as well as the morphology (density, thickness, disorder). Based on effective media approximations, the perfect VACNT-based absorber is supposed to have very low density (denote as *f*) and high alignment (denote as *x*). However, in practice, the vertical alignment is realized through a self-assembly process depending on the density, and thus low *f* and high *x* values cannot be achieved simultaneously as *f* and *x* are positively correlated with each other. Previous strategies to decrease the reflectance of VACNTs include CF_4 plasma etching on the top surface[48] or adding carbon soot,[10] which forms hierarchical
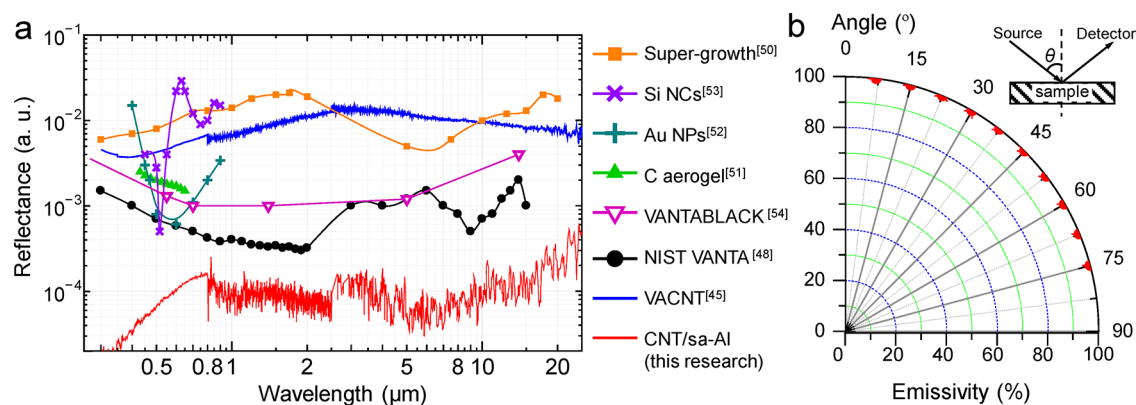
Figure 5. (a) Reflectance of CNT/sa-Al hierarchical structures over visible, near-IR and mid-IR wavelength range, compared with the reflectance of VACNT forest grown on Si/SiO₂ wafer (data taken from ref 45), NIST VANTA CNT structures (data taken from ref 48), supergrowth SWNT forest (data taken from ref 50), carbon aerogel (data taken from ref 51), Au nanoparticle arrays (data taken from ref 52), Si nanocylinder arrays (data taken from ref 53) and VANTABLACK (data taken from ref 54). (b) Angular dependence of average emissivity of CNT/sa-Al hierarchical structure over visible and NIR wavelength range.

structures for light trapping. These strategies, although effective, create large number of defects which would cause overheating (hot spot effect) and even ignition of the VACNTs. Moreover, the fragility of CNT forest requires effective integration with mechanically robust substrates. Therefore, VACNTs are not used in modern gravitational-wave detectors under development like LIGO, Virgo, and KAGRA.[49]

The CNT/sa-Al structure composed of the upper CNT layer with bimodal pore size distribution and the bottom layer of Al nanowire network is an ideal hierarchical structure of light trapping for broadband absorber. Figure 5a shows the surface spectral reflectance of the CNT/sa-Al structure, compared with that of our reference CNT forest grown on a Si wafer,[45] NIST VANTA,[48] supergrowth SWNT forest,[50] carbon aerogel,[51] gold nanoparticles,[52] silicon nanocylinder array-based Mie resonator,[53] and VANTABLACK[54] over the wavelength range from ultraviolet to terahertz using UV–vis–NIR spectroscopy and Fourier-transform infrared spectroscopy. The CNT/sa-Al shows record-low reflectance of 1×10^{-5} over the UV, visible, infrared and terahertz range, which is 2 orders of magnitude lower than the reference VACNTs grown on Si substrate, and 1 order of magnitude lower than the state-of-the-art superblack material NIST VANTA (CF₄-etched VACNTs). More importantly, the CNT/sa-Al structure shows omnidirectional blackbody optical absorption in the visible and NIR range as shown in Figure 5b. The extremely low spectrum and angular reflectance of the CNT/sa-Al substrate could be beneficial for applications in solar steam generation,[27] near-infrared sensing,[55] and various space science applications including astronomy detectors[56] and straylight shades.[57]

CONCLUSION

In this work, a surface activation process is demonstrated for the removal of native oxide on metallic substrate which significantly improves the catalytic activity for direct synthesis of high-yield and high-quality CNTs on Al and Al alloy substrates. The surface activation process introduces nanoscale roughness that enhances catalytic activity and removes the native oxide layer to realize direct contact between CNTs and the metallic Al substrate. The surface treatment improved both the growth yield and quality of the CNTs because of three reasons: (a) the Al nanostructures formed by surface activation

are mesoporous which significantly increases the catalyst loading; (b) the surface-activated Al nanostructures not only serve as active sites, but also enhance hydrogen adsorption and spillover onto catalysts; and (c) the removal of the oxide allows sufficient element diffusion and thus results in the formation of the Al-rich intermetallic compounds that are reported to be effective catalytic-active centers for dehydrogenation. Moreover, the exposed metallic Al surface serves as a solid-state reducing agent for the catalyst during the annealing process.

The surface activation process introduced herein is intrinsically scalable, as both the surface activation process and the direct synthesis of CNTs can be deployed in a roll-to-roll fashion using solution baths. The oxide-free CNT-Al structure features with high surface area, enhanced charge transfer and record-low optical and IR wavelength surface reflection, which enables multifunctionality for applications in energy storage devices, solar cells, thermal/electrical interconnects, solar desalination, and space science instruments. Moreover, the surface activation process can be used to create nanostructured surface for various catalysis applications, such as CO_2 and oxygen reduction reaction,[58] fuel cells,[59] etc.

ASSOCIATED CONTENT

⑤ Supporting Information

The Supporting Information is available free of charge on the ACS Publications website at DOI: 10.1021/acsami.9b08290.

Figures S1–S9 as described in the text (PDF)

AUTHOR INFORMATION

Corresponding Authors

*Email: cuikehang@sjtu.edu.cn.
*Email: wardle@mit.edu.

ORCID ⓘ

Kehang Cui: 0000-0002-1768-0845

Notes

The authors declare no competing financial interest.

■ REFERENCES

(1) Rao, R.; Pint, C. L.; Islam, A. E.; Weatherup, R. S.; Hofmann, S.; Meshot, E. R.; Wu, F.; Zhou, C.; Dee, N.; Amama, P. B.; Carpena-Nuñez, J.; Shi, W.; Plata, D. L.; Penev, E. S.; Yakobson, B. I.; Balbuena, P. B.; Bichara, C.; Futaba, D. N.; Noda, S.; Shin, H.; Kim, K. S.; Simard, B.; Mirri, F.; Pasquali, M.; Fornasiero, F.; Kauppinen, E. I.; Arnold, M.; Cola, B. A.; Nikolaev, P.; Arepalli, S.; Cheng, H.-M.; Zakharov, D. N.; Stach, E. A.; Zhang, J.; Wei, F.; Terrones, M.; Geohegan, D. B.; Maruyama, B.; Maruyama, S.; Li, Y.; Adams, W. W.; Hart, A. J. Carbon Nanotubes and Related Nanomaterials: Critical Advances and Challenges for Synthesis toward Mainstream Commercial Applications. *ACS Nano* **2018**, *12*, 11756−11784.

(2) Cui, K.; Qian, Y.; Jeon, I.; Anisimov, A.; Matsuo, Y.; Kauppinen, E. I.; Maruyama, S. Scalable and Solid-State Redox Functionalization of Transparent Single-Walled Carbon Nanotube Films for Highly Efficient and Stable Solar Cells. *Adv. Energy Mater.* **2017**, *7*, 1700449.

(3) Aitola, K.; Domanski, K.; Correa Baena, J. P.; Sveinbjörnsson, K.; Saliba, M.; Abate, A.; Grätzel, M.; Kauppinen, E.; Johansson, E. M. J.; Tress, W.; Hagfeldt, A.; Boschloo, G. High Temperature-Stable Perovskite Solar Cell Based on Low-Cost Carbon Nanotube Hole Contact. *Adv. Mater.* **2017**, *29*, 1606398.

(4) Cui, K.; Maruyama, S. Multifunctional Graphene and Carbon Nanotube Films for Planar Heterojunction Solar Cells. *Prog. Energy Combust. Sci.* **2019**, *70*, 1−21.

(5) Liang, X.; Rangom, Y.; Kwok, C. Y.; Pang, Q.; Nazar, L. F. Interwoven Mxene Nanosheet/Carbon-Nanotube Composites as Li−S Cathode Hosts. *Adv. Mater.* **2017**, *29*, 1603040.

(6) Zou, M.; Zhao, W.; Wu, H.; Zhang, H.; Xu, W.; Yang, L.; Wu, S.; Wang, Y.; Chen, Y.; Xu, L.; Cao, A. Single Carbon Fibers with a Macroscopic-Thickness, 3d Highly Porous Carbon Nanotube Coating. *Adv. Mater.* **2018**, *30*, 1704419.

(7) Mao, Y.; Li, G.; Guo, Y.; Li, Z.; Liang, C.; Peng, X.; Lin, Z. Foldable Interpenetrated Metal-Organic Frameworks/Carbon Nanotubes Thin Film for Lithium−Sulfur Batteries. *Nat. Commun.* **2017**, *8*, 14628.

(8) Lin, Z.; Zeng, Z.; Gui, X.; Tang, Z.; Zou, M.; Cao, A. Carbon Nanotube Sponges, Aerogels, and Hierarchical Composites: Synthesis, Properties, and Energy Applications. *Adv. Energy Mater.* **2016**, *6*, 1600554.

(9) Chen, C.; Li, Y.; Song, J.; Yang, Z.; Kuang, Y.; Hitz, E.; Jia, C.; Gong, A.; Jiang, F.; Zhu, J. Y.; Yang, B.; Xie, J.; Hu, L. Highly Flexible and Efficient Solar Steam Generation Device. *Adv. Mater.* **2017**, *29*, 1701756.

(10) Yin, Z.; Wang, H.; Jian, M.; Li, Y.; Xia, K.; Zhang, M.; Wang, C.; Wang, Q.; Ma, M.; Zheng, Q.-s.; Zhang, Y. Extremely Black Vertically Aligned Carbon Nanotube Arrays for Solar Steam Generation. *ACS Appl. Mater. Interfaces* **2017**, *9*, 28596−28603.

(11) Hu, X.; Xu, W.; Zhou, L.; Tan, Y.; Wang, Y.; Zhu, S.; Zhu, J. Tailoring Graphene Oxide-Based Aerogels for Efficient Solar Steam Generation under One Sun. *Adv. Mater.* **2017**, *29*, 1604031.

(12) Yu, W.; Duan, Z.; Zhang, G.; Liu, C.; Fan, S. Effect of an Auxiliary Plate on Passive Heat Dissipation of Carbon Nanotube-Based Materials. *Nano Lett.* **2018**, *18*, 1770−1776.

(13) Subramaniam, C.; Yamada, T.; Kobashi, K.; Sekiguchi, A.; Futaba, D. N.; Yumura, M.; Hata, K. One Hundred Fold Increase in Current Carrying Capacity in a Carbon Nanotube−Copper Composite. *Nat. Commun.* **2013**, *4*, 2202.

(14) Lee, J.; Stein, I. Y.; Kessler, S. S.; Wardle, B. L. Aligned Carbon Nanotube Film Enables Thermally Induced State Transformations in Layered Polymeric Materials. *ACS Appl. Mater. Interfaces* **2015**, *7*, 8900−8905.

(15) Gorbatikh, L.; Wardle, B. L.; Lomov, S. V. Hierarchical Lightweight Composite Materials for Structural Applications. *MRS Bull.* **2016**, *41*, 672−677.

(16) Yang, Y.; Kushima, A.; Han, W.; Xin, H.; Li, J. Liquid-Like, Self-Healing Aluminum Oxide During Deformation at Room Temperature. *Nano Lett.* **2018**, *18*, 2492−2497.

(17) Cao, Q.; Han, S.-J.; Tersoff, J.; Franklin, A. D.; Zhu, Y.; Zhang, Z.; Tulevski, G. S.; Tang, J.; Haensch, W. End-Bonded Contacts for Carbon Nanotube Transistors with Low, Size-Independent Resistance. *Science* **2015**, *350*, 68−72.

(18) Kaur, S.; Raravikar, N.; Helms, B. A.; Prasher, R.; Ogletree, D. F. Enhanced Thermal Transport at Covalently Functionalized Carbon Nanotube Array Interfaces. *Nat. Commun.* **2014**, *5*, 3082.

(19) Hao, M.; Kumar, A.; Hodson, S. L.; Zemlyanov, D.; He, P.; Fisher, T. S. Brazed Carbon Nanotube Arrays: Decoupling Thermal Conductance and Mechanical Rigidity. *Adv. Mater. Interfaces* **2017**, *4*, 1601042.

(20) Sun, W.; Zhu, Y.; Marceau, R.; Wang, L.; Zhang, Q.; Gao, X.; Hutchinson, C. Precipitation Strengthening of Aluminum Alloys by Room-Temperature Cyclic Plasticity. *Science* **2019**, *363*, 972−975.

(21) Zoican Loebick, C.; Podila, R.; Reppert, J.; Chudow, J.; Ren, F.; Haller, G. L.; Rao, A. M.; Pfefferle, L. D. Selective Synthesis of Subnanometer Diameter Semiconducting Single-Walled Carbon Nanotubes. *J. Am. Chem. Soc.* **2010**, *132*, 11125−11131.

(22) Sakurai, S.; Nishino, H.; Futaba, D. N.; Yasuda, S.; Yamada, T.; Maigne, A.; Matsuo, Y.; Nakamura, E.; Yumura, M.; Hata, K. Role of Subsurface Diffusion and Ostwald Ripening in Catalyst Formation for Single-Walled Carbon Nanotube Forest Growth. *J. Am. Chem. Soc.* **2012**, *134*, 2148−2153.

(23) Tsuji, T.; Hata, K.; Futaba, D. N.; Sakurai, S. Unexpected Efficient Synthesis of Millimeter-Scale Single-Wall Carbon Nanotube Forests Using a Sputtered Mgo Catalyst Underlayer Enabled by a Simple Treatment Process. *J. Am. Chem. Soc.* **2016**, *138*, 16608−16611.

(24) Hu, M.; Murakami, Y.; Ogura, M.; Maruyama, S.; Okubo, T. Morphology and Chemical State of Co−Mo Catalysts for Growth Of single-Walled Carbon Nanotubes Vertically Aligned on Quartz Substrates. *J. Catal.* **2004**, *225*, 230−239.

(25) Reit, R.; Nguyen, J.; Ready, W. J. Growth Time Performance Dependence of Vertically Aligned Carbon Nanotube Supercapacitors Grown on Aluminum Substrates. *Electrochim. Acta* **2013**, *91*, 96−100.

(26) Zhang, B.; Wang, J.; Wu, B.; Guo, X. W.; Wang, Y. J.; Chen, D.; Zhang, Y. C.; Du, K.; Oguzie, E. E.; Ma, X. L. Unmasking Chloride Attack on the Passive Film of Metals. *Nat. Commun.* **2018**, *9*, 2559.

(27) Zhou, L.; Tan, Y.; Wang, J.; Xu, W.; Yuan, Y.; Cai, W.; Zhu, S.; Zhu, J. 3d Self-Assembly of Aluminium Nanoparticles for Plasmon-Enhanced Solar Desalination. *Nat. Photonics* **2016**, *10*, 393.

(28) Miura, S.; Yoshihara, Y.; Asaka, M.; Hasegawa, K.; Sugime, H.; Ota, A.; Oshima, H.; Noda, S. Millimeter-Tall Carbon Nanotube Arrays Grown on Aluminum Substrates. *Carbon* **2018**, *130*, 834−842.

(29) Liatard, S.; Benhamouda, K.; Fournier, A.; Ramos, R.; Barchasz, C.; Dijon, J. Vertically-Aligned Carbon Nanotubes on Aluminum as a Light-Weight Positive Electrode for Lithium-Polysulfide Batteries. *Chem. Commun.* **2015**, *51*, 7749−7752.

(30) Zhang, Z.; Chen, X.; Lagally, M. G. Bonding-Geometry Dependence of Fractal Growth on Metal Surfaces. *Phys. Rev. Lett.* **1994**, *73*, 1829−1832.

(31) Ferrari, A. C.; Robertson, J. Interpretation of Raman Spectra of Disordered and Amorphous Carbon. *Phys. Rev. B: Condens. Matter Mater. Phys.* **2000**, *61*, 14095−14107.

(32) Ferrari, A. C.; Robertson, J. Origin of the 1150 Cm-1 Raman Mode in Nanocrystalline Diamond. *Phys. Rev. B: Condens. Matter Mater. Phys.* **2001**, *63*, 121405.

(33) Hafner, J.; Krajčí, M. Surfaces of Complex Intermetallic Compounds: Insights from Density Functional Calculations. *Acc. Chem. Res.* **2014**, *47*, 3378−3384.

(34) Armbrüster, M.; Kovnir, K.; Friedrich, M.; Teschner, D.; Wowsnick, G.; Hahne, M.; Gille, P.; Szentmiklósi, L.; Feuerbacher, M.; Heggen, M.; Girgsdies, F.; Rosenthal, D.; Schlögl, R.; Grin, Y. Al13fe4 as a Low-Cost Alternative for Palladium in Heterogeneous Hydrogenation. *Nat. Mater.* **2012**, *11*, 690.

(35) Jaiswal, G.; Landge, V. G.; Jagadeesan, D.; Balaraman, E. Iron-Based Nanocatalyst for the Acceptorless Dehydrogenation Reactions. *Nat. Commun.* **2017**, *8*, 2147.

(36) Pitkänen, O.; Järvinen, T.; Cheng, H.; Lorite, G. S.; Dombovari, A.; Rieppo, L.; Talapatra, S.; Duong, H. M.; Tóth, G.; Juhász, K. L.; Kónya, Z.; Kukovecz, A.; Ajayan, P. M.; Vajtai, R.; Kordás, K. On-Chip Integrated Vertically Aligned Carbon Nanotube Based Super- and Pseudocapacitors. *Sci. Rep.* **2017**, *7*, 16594.

(37) Pitkänen, O.; Lorite, G. S.; Shi, G.; Rautio, A.-R.; Uusimäki, A.; Vajtai, R.; Tóth, G.; Kordás, K. The Effect of Al Buffer Layer on the Catalytic Synthesis of Carbon Nanotube Forests. *Top. Catal.* **2015**, *58*, 1112−1118.

(38) Prins, R. Hydrogen Spillover. Facts and Fiction. *Chem. Rev.* **2012**, *112*, 2714−2738.

(39) Cheng, H.; Chen, L.; Cooper, A. C.; Sha, X.; Pez, G. P. Hydrogen Spillover in the Context of Hydrogen Storage Using Solid-State Materials. *Energy Environ. Sci.* **2008**, *1*, 338−354.

(40) Fiawoo, M. F. C.; Bonnot, A. M.; Amara, H.; Bichara, C.; Thibault-Pénisson, J.; Loiseau, A. Evidence of Correlation between Catalyst Particles and the Single-Wall Carbon Nanotube Diameter: A First Step Towards Chirality Control. *Phys. Rev. Lett.* **2012**, *108*, 195503.

(41) Sourmail, T. Near Equiatomic FeCo Alloys: Constitution, Mechanical and Magnetic Properties. *Prog. Mater. Sci.* **2005**, *50*, 816−880.

(42) Cui, K.; Kumamoto, A.; Xiang, R.; An, H.; Wang, B.; Inoue, T.; Chiashi, S.; Ikuhara, Y.; Maruyama, S. Synthesis of Subnanometer-Diameter Vertically Aligned Single-Walled Carbon Nanotubes with Copper-Anchored Cobalt Catalysts. *Nanoscale* **2016**, *8*, 1608−1617.

(43) Chiang, W.-H.; Mohan Sankaran, R. Linking Catalyst Composition to Chirality Distributions of as-Grown Single-Walled Carbon Nanotubes by Tuning Ni_xFe_{1-x} Nanoparticles. *Nat. Mater.* **2009**, *8*, 882.

(44) Hou, B.; Wu, C.; Inoue, T.; Chiashi, S.; Xiang, R.; Maruyama, S. Extended Alcohol Catalytic Chemical Vapor Deposition for Efficient Growth of Single-Walled Carbon Nanotubes Thinner Than (6,5). *Carbon* **2017**, *119*, 502−510.

(45) Meshot, E. R.; Plata, D. L.; Tawfick, S.; Zhang, Y.; Verploegen, E. A.; Hart, A. J. Engineering Vertically Aligned Carbon Nanotube Growth by Decoupled Thermal Treatment of Precursor and Catalyst. *ACS Nano* **2009**, *3*, 2477−2486.

(46) Meng, J.; Guo, H.; Niu, C.; Zhao, Y.; Xu, L.; Li, Q.; Mai, L. Advances in Structure and Property Optimizations of Battery Electrode Materials. *Joule* **2017**, *1*, 522−547.

(47) Yu, Z.; Tetard, L.; Zhai, L.; Thomas, J. Supercapacitor Electrode Materials: Nanostructures from 0 to 3 Dimensions. *Energy Environ. Sci.* **2015**, *8*, 702−730.

(48) Lehman, J.; Sanders, A.; Hanssen, L.; Wilthan, B.; Zeng, J.; Jensen, C. Very Black Infrared Detector from Vertically Aligned Carbon Nanotubes and Electric-Field Poling of Lithium Tantalate. *Nano Lett.* **2010**, *10*, 3261−3266.

(49) Akutsu, T.; Saito, Y.; Sakakibara, Y.; Sato, Y.; Niwa, Y.; Kimura, N.; Suzuki, T.; Yamamoto, K.; Tokoku, C.; Koike, S.; Chen, D.; Zeidler, S.; Ikeyama, K.; Ariyama, Y. Vacuum and Cryogenic Compatible Black Surface for Large Optical Baffles in Advanced Gravitational-Wave Telescopes. *Opt. Mater. Express* **2016**, *6*, 1613−1626.

(50) Mizuno, K.; Ishii, J.; Kishida, H.; Hayamizu, Y.; Yasuda, S.; Futaba, D. N.; Yumura, M.; Hata, K. A Black Body Absorber from Vertically Aligned Single-Walled Carbon Nanotubes. *Proc. Natl. Acad. Sci. U. S. A.* **2009**, *106*, 6044−6047.

(51) Sun, W.; Du, A.; Feng, Y.; Shen, J.; Huang, S.; Tang, J.; Zhou, B. Super Black Material from Low-Density Carbon Aerogels with Subwavelength Structures. *ACS Nano* **2016**, *10*, 9123−9128.

(52) Kwon, N.; Oh, H.; Kim, R.; Sinha, A.; Kim, J.; Shin, J.; Chon, J. W. M.; Lim, B. Direct Chemical Synthesis of Plasmonic Black Colloidal Gold Superparticles with Broadband Absorption Properties. *Nano Lett.* **2018**, *18*, 5927.

(53) Spinelli, P.; Verschuuren, M. A.; Polman, A. Broadband Omnidirectional Antireflection Coating Based on Subwavelength Surface Mie Resonators. *Nat. Commun.* **2012**, *3*, 692.

(54) Vantablack Technical Data Sheet from Surrey Nano-systems.www.surreynanosystems.com (retrieved July 14, 2019).

(55) Akselrod, G. M.; Huang, J.; Hoang, T. B.; Bowen, P. T.; Su, L.; Smith, D. R.; Mikkelsen, M. H. Large-Area Metasurface Perfect Absorbers from Visible to near-Infrared. *Adv. Mater.* **2015**, *27*, 8028−8034.

(56) Lehman, J.; Yung, C.; Tomlin, N.; Conklin, D.; Stephens, M. Carbon Nanotube-Based Black Coatings. *Appl. Phys. Rev.* **2018**, *5*, No. 011103.

(57) Iyengar, V. V.; Nayak, B. K.; Gupta, M. C. Ultralow Reflectance Metal Surfaces by Ultrafast Laser Texturing. *Appl. Opt.* **2010**, *49*, 5983−5988.

(58) Guo, D.; Shibuya, R.; Akiba, C.; Saji, S.; Kondo, T.; Nakamura, J. Active Sites of Nitrogen-Doped Carbon Materials for Oxygen Reduction Reaction Clarified Using Model Catalysts. *Science* **2016**, *351*, 361−365.

(59) Chen, Y.; deGlee, B.; Tang, Y.; Wang, Z.; Zhao, B.; Wei, Y.; Zhang, L.; Yoo, S.; Pei, K.; Kim, J. H.; Ding, Y.; Hu, P.; Tao, F. F.; Liu, M. A Robust Fuel Cell Operated on Nearly Dry Methane at 500 °C Enabled by Synergistic Thermal Catalysis and Electrocatalysis. *Nat. Energy* **2018**, *3*, 1042−1050.